

Contents lists available at ScienceDirect

### Journal of Alloys and Compounds

journal homepage: http://www.elsevier.com/locate/jalcom



## Formation of cuboidal B2 nanoprecipitates and microstructural evolution in the body-centered-cubic $Al_{0.7}NiCoFe_{1.5}Cr_{1.5}$ high-entropy alloy



Jiamiao Hao <sup>a</sup>, Yue Ma <sup>a</sup>, Qing Wang <sup>a, \*</sup>, Chuan Zhang <sup>b</sup>, Chunling Li <sup>a</sup>, Chuang Dong <sup>a</sup>, Qiang Song <sup>c</sup>, Peter K. Liaw <sup>d</sup>

- <sup>a</sup> Key Laboratory of Materials Modification by Laser, Ion and Electron Beams (Ministry of Education), School of Materials Science and Engineering, Dalian University of Technology, Dalian, 116024, China
- <sup>b</sup> CompuTherm, LLC, Middleton, WI 53562, USA
- <sup>c</sup> School of Materials Science and Engineering, Shandong University of Science and Technology, Oingdao, 266590, China
- <sup>d</sup> Department of Materials Science and Engineering, University of Tennessee, Knoxville, TN, 37996, USA

#### ARTICLE INFO

# Article history: Received 16 September 2018 Received in revised form 24 November 2018 Accepted 28 November 2018 Available online 29 November 2018

Keywords: High-entropy alloys Coherent precipitation Microstructural evolution Phase transformation Strengthening mechanism

#### ABSTRACT

The present work primarily investigated the formation of coherent cuboidal B2 nanoprecipitates in body-centered-cubic (BCC) Al $_{0.7}$ NiCoFe $_{1.5}$ Cr $_{1.5}$  high-entropy alloy (HEA) and its microstructural evolution with temperature. Alloy samples were prepared by suction-cast processing and then heat-treated at different temperatures of 673–1273 K for 2 h, respectively. It was found that the coherent microstructure with cuboidal B2 nanoprecipitates in BCC matrix can be formed in the as-cast state and be stabilized up to 823 K with a particle size of 60–120 nm. Even after being heat-treated at 773 K for 1080 h, the cuboidal B2 nanoprecipitates were still stabilized without any coarsening. It was due to a moderate lattice misfit ( $\varepsilon$  = 0.4–0.5%) that favored the formation of coherent cuboidal B2 nanoprecipitates, resulting in a good compressive mechanical property. Meanwhile, the Fe/Cr-rich  $\sigma$  phase appeared and dominated after the treatment at 873 K, causing heavy brittleness. The face-centered-cubic (FCC) phase appeared at 973 K and became dominant above 1173 K, which softened the alloy. In addition, the thermodynamic calculations were carried out for further understanding the microstructural evolution with temperature. The influence of microstructures constituted by different phases on mechanical properties was studied, in which high strength caused by cuboidal B2 nanoprecipitates was discussed in light of the precipitation-strengthening mechanism.

© 2018 Elsevier B.V. All rights reserved.

#### 1. Introduction

High-entropy alloys (HEAs) have attracted increasing interest due to their simple crystalline structures and the resultant prominent mechanical properties (e.g., high strength and toughness), as well as the superior resistances to creep, fatigue and corrosion at elevated temperatures [1–12]. They could be formed in diverse multi-component alloy systems with principal elements mixed by equi-molar, near equi-molar, or even non equi-molar ratios [13,14]. For instance, the single-phase face-centered-cubic (FCC) CoCrFe-NiMn HEA exhibited excellent properties with higher tensile

\* Corresponding author. E-mail address: wangq@dlut.edu.cn (Q. Wang). strength and fracture toughness than traditional stainless steels at cryogenic temperatures [15]. The addition of the Al element into FCC HEAs constituted by the late transition metals (TMs) was always used to change phase structures of Al-TM HEAS [16–21]. It was fascinating that the coherent precipitation of ordered Ni<sub>3</sub>Al (L1<sub>2</sub>-Cu<sub>3</sub>Au type) nanoparticles in the FCC matrix can enhance significantly the strength of low Al-contained FCC HEAs, in a manner similar to that in Ni-based superalloys [22–24]. Further increasing the Al content up to a high level, the FCC matrix of HEAs will transform into the body-centered-cubic (BCC) structure [16]. Besides high strength, the outstanding oxidation- and corrosion-resistant properties at high temperatures (HTs) have been achieved in refractory BCC HEAs, which are generally composed of early transition metals [25–29]. Thereof, HEAs will be of great potential for applications in extreme environments.

It was emphasized that the phase formations in HEAs are metastable and are prone to be affected by heat treatment or deformation, resulting in phase decomposition and microstructure transformation [30-33]. For instance, the CoCrFeMnNi HEA exhibited a single FCC solid-solution structure after homogenization at 1473 K for 2 days, which could remain after a subsequent annealing at 1173 K even for 500 days. However, the FCC phase became unstable when annealing at relatively-lower temperatures, in which a Fe/Cr-rich sigma phase appeared at 1073 K, and other phases, like Ni/Mn-rich L1<sub>0</sub> (CuAu-type), Fe/Co-rich B2 (CsCl-type), and a Cr-rich BCC- $\alpha'$ , could precipitate at 773 K-annealing [30]. Similarly, cold rolling with a large strain deformation (~80%) could also induce phase transformation from FCC to both  $\sigma$  and  $\alpha'$  phases in this HEA, as a result of an embrittlement [31]. In Al-contained Al-TM HEAs, it is much easier to produce brittle phases during the heat treatment. After annealing at 923–1248 K for 3 h, the brittle  $\sigma$ phase precipitated from the BCC matrix in AlCoCrFeNi HEA, and it would be transformed back to the BCC when annealing at a higher temperature of 1373 K [32]. Besides the experimental observations, the thermodynamic calculation of phase diagrams (CALPHAD) approach has been widely accepted and played a more and more important role in the design and development of multi-component HEAs, which can predict the phase equilibrium and phase transformation well at present [34-36]. For example, the thermodynamic calculations were confronted to the experimental results for providing the insight into understanding the formation of secondary phases and their effect on mechanical properties of the  $Al_x$ CoCrFeNi (x = 0.3, 0.5, and 0.7) HEAs at elevated temperatures [37]. So, the microstructural stability of HEAs is of crucial importance for their applications at HTs, especially for high-strength Al-TMs HEAs. However, it has received much less attention up to now, which needs further elaborate investigations.

In BCC-based Al-TM HEAs particularly, the BCC solid solution matrix is always coherently-accompanied by its ordered B2 superstructure (a Ni- and Al-rich phase) [16-21]. However, the BCC and B2 phases often form a weave-like microstructure due to an excessive addition of Al, leading to heavy brittleness in spite of high strength [16-21]. The coherent precipitation of spherical or cuboidal B2 nanoparticles in the BCC matrix is expected to ensure HT mechanical properties of Al-TM HEAs, similar to the microstructure of FCC and L12 phase in Ni-based superalloys [22-24]. Actually, it is difficult to achieve such coherent microstructures, since it is sensitive to the change of the Al content alone. In our recent work, we obtained cuboidal B2 nanoprecipitates in the BCC matrix of Al-TM HEAs with the composition formula of Al<sub>2</sub>M<sub>14</sub>, where Al is fixed and M represents different mutations of Ni, Co, Fe, and Cr [38]. The Al<sub>2</sub>M<sub>14</sub> was designed with the guide of a cluster formula approach through mutating the combinations of TMs, rather than the Al. Typically, it is due to the coherent precipitation of cuboidal B2 nanoparticles in the BCC matrix of the HEA with  $M = NiCoFe_2Cr$  (i.e.,  $Al_{0.7}NiCoFe_2Cr$ ) that results in a prominent mechanical property with a high ultimate tensile strength of 1223 MPa and an elongation of 7.9% [39]. Besides, the BCC Al<sub>0.7</sub>Ni-CoFeCr<sub>2</sub> HEA with M = NiCoFeCr<sub>2</sub> also possessed similar cuboidal B2 nanoprecipitates and exhibited a much higher strength (the compressive yield strength being 1718 MPa) [38]. It is noted that microstructural stabilities at HTs of this kind of coherent microstructure with cuboidal B2 nanoprecipitates in the BCC matrix have not been investigated until now.

Therefore, the present work aims at primarily the formation of cuboidal B2 nanoprecipitates and the microstructural evolution with temperature. First, we still apply the cluster formula of  $Al_2M_{14}$  to design the alloy composition, in which the combination of M is  $M = Ni_1Co_1Fe_{1.5}Cr_{1.5}$ , resulting in the composition of

Al<sub>0.7</sub>NiCoFe<sub>1.5</sub>Cr<sub>1.5</sub> (Al<sub>12.5</sub>Ni<sub>17.5</sub>Co<sub>17.5</sub>Fe<sub>26.25</sub>Cr<sub>26.25</sub> in atomic percent, at. %). We calculated the valance electron concentration (VEC) of the M, and found that the VEC = 8 of M is equal to that of the Fe element, where the VEC values of TMs are  $VEC_{Cr} = 6$ ,  $VEC_{Fe} = 8$ ,  $VEC_{Co} = 9$ , and  $VEC_{Ni} = 10$ , respectively. It means that this alloy could be regarded as an Al-Fe pseudo-binary alloy since M is similar to Fe. In the Fe-Al binary alloy diagram, the BCC  $\alpha$ -Fe solid solution is coherent with its ordered B2-FeAl phase [40]. Thus, the formation of cuboidal B2 nanoprecipitates will be verified in the designed Al<sub>0.7</sub>NiCoFe<sub>1.5</sub>Cr<sub>1.5</sub> HEA, and the shape of B2 precipitates will be discussed in light of the lattice misfit between BCC and B2 phases. Second, the microstructural evolution of this HEA with temperature, i.e., the microstructural stability will be focused on from the viewpoints of both experiments and thermodynamic calculations. Finally, the influence of the microstructures constituted by different phases on mechanical properties will be investigated, and the precipitation strengthening mechanism of B2 nanoparticles will be addressed.

#### 2. Experimental

The  $Al_{0.7}$ NiCoFe<sub>1.5</sub>Cr<sub>1.5</sub> HEA was prepared by means of arc melting and copper-mold suction-casting into a  $\phi 6$  mm rod under an argon atmosphere. The purities (weight percent, wt. %) of the raw metals are 99.99% for Al, Co, and 99.99% for Fe, Cr, and 99.9% for Ni. These ingots with a weight of about 14 g were re-melted at least five times to ensure the chemical homogeneity before suction-casting. Alloy samples were then heat-treated at 673 K, 773 K, 823 K, 873 K, 973 K, 1073 K, 1173 K, and 1273 K for 2 h, respectively, followed by water quenching. Especially, the treatment time at 773 K was prolonged up to 24 h, 216 h, 720 h, and 1080 h, respectively, followed by water-quenching.

The crystalline structures of the as-cast and heat-treated alloy samples were identified, using a Bruker D8 X-ray diffractometer (XRD) with a Cu- $K_{\alpha}$  radiation ( $\lambda = 0.15406 \, \text{nm}$ ) and a scanning speed of 2°/min, in which an external standard method was applied to calculate the lattice constants of phases [41]. The microstructure was examined, using the Olympus optical microscopy (OM), Zeiss Supra 55 scanning electron microscope (SEM), and JEOL-JEM-2100F field emission transmission electron microscope (TEM) equipped with a JEM2100F FEG scanning transmission electron microscope (STEM). Alloy samples for OM and SEM observations were mechanically ground, polished (using the W1.0 diamond paste for the final polish) and then etched in a mixed solution of 5 g  $FeCl_3 \cdot 6H_2O + 25 \text{ ml HCl} + 25 \text{ ml C}_2H_5OH$ . The TEM samples were initially ground to a thickness of about 50 μm, punched into disks of 3 mm in diameter, and then thinned by twin-jet electro-polishing with a voltage of  $35-45\,V$  and in a solution of  $10\%\,HClO_4\,+\,90\%$ C<sub>2</sub>H<sub>5</sub>OH (volume fraction) at about 243 K. The particle size was defined as the length of cuboidal precipitates (i.e.,  $r = \sqrt{\text{area}}$  for the cuboidal particles and  $r = 2\sqrt{\text{area}/\pi}$  for the spheroidal particles) and the standard error (SE) in r was obtained using  $SE = \sigma/\sqrt{N}$ where  $\sigma$  is the standard deviation of precipitate sizes, and N is the number of precipitates. The volume fraction f of precipitates was estimated by  $f = A_f$ , where  $A_f$  is the projected areal fraction of precipitates. At least 6 TEM or SEM micrographs from different regions were taken in determining r and f, in which the values of precipitate area were obtained with the ImageJ software. Chemical compositions of phases in differently-treated samples were measured by STEM with the Oxford INCA software. Besides, the CALPHAD approach was carried out to predict the phase constitutions and fractions with temperature by using the Pan-dat™ [42] software and PanHEA database.

The uniaxial compressive tests were conducted on an 810

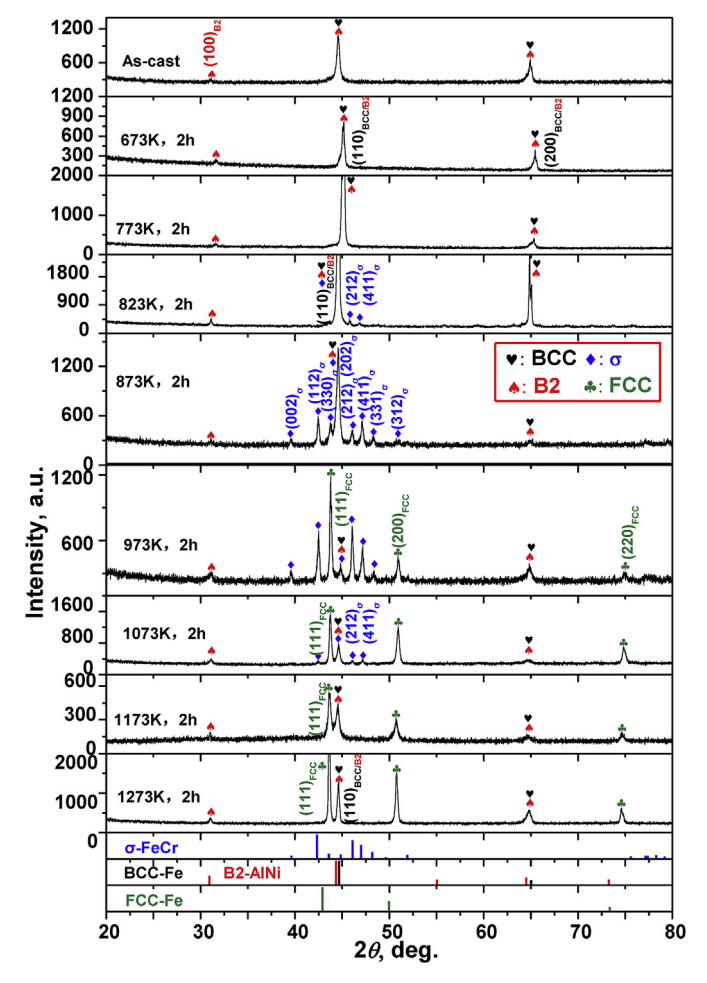


Fig. 1. XRD patterns of the  $Al_{0.7}$ NiCoFe<sub>1.5</sub>Cr<sub>1.5</sub> HEA in the as-cast and heat-treated states within a temperature range of 673–1273 K for 2 h.

Material Test System (MTS) universal test machine with a strain rate of  $1 \times 10^{-3}$ /s. The machine stiffness was first evaluated to compensate the true strain. It was measured by compressing the

same-sized 310S stainless steel sample with a known Young's modulus of 205 GPa, from which the force-displacement curve was obtained, and the machine stiffness was deduced after subtracting the elastic contribution from the 310S sample. The measured machine stiffness was subsequently integrated in the compressive strain to properly convert the engineering compression to true compression. At least three cylindrical samples with a size of  $\varphi3\times 6$  mm were tested for each treatment state. Microhardness of both as-cast and heat-treated samples was tested with a HVS-1000 Vickers hardness tester under a load of 500 g for 20 s, in which at least 12 indents were taken to obtain an average value.

#### 3. Results

#### 3.1. Microstructural characteristics

The XRD patterns of the Al<sub>0.7</sub>NiCoFe<sub>1.5</sub>Cr<sub>1.5</sub> HEA in the as-cast state and after heat treatments at different temperatures are presented in Fig. 1. The as-cast HEA is composed of the BCC solid solution and the ordered B2 phase (characterized by a weak (100) diffraction peak). Heat treatments at T < 823 K do not change the phase constitution, still retaining the BCC and B2 structures. While the  $\sigma$  phase with a tetragonal structure begins to appear from the BCC/B2 matrix when treated at 823 K, and it will be dominant at 873 K. With elevating the temperature to 973 K, an FCC phase appears and will be dominant at 1173 K, besides the  $\sigma$ . Further increasing temperature up to 1173–1273 K, the  $\sigma$  phase disappears, and a dual-phase combination of (FCC + BCC/B2) dominates in alloy samples. It is noted that the diffraction peaks related to BCC and B2 phases existed within a large temperature region from room temperature to 1273 K. The data summary, including the phase constitution and lattice constants of these phases, of the Al<sub>0.7</sub>Ni-CoFe<sub>1.5</sub>Cr<sub>1.5</sub> HEA in the as-cast state and after heat treatments at different temperatures are listed in Table 1.

The microstructural evolution of this alloy with temperature can be clearly identified by the OM and SEM morphological images of as-cast and heat-treated states at different temperatures, as seen in Fig. 2. The as-cast alloy exhibits a coarse columnar dendrite microstructure (Fig. 2(a)), which is constituted by a large amount of cuboidal B2 nanoparticles coherently-precipitated in the BCC matrix (Fig. 2(b)). It is noted that after heat treatments at different temperatures of 673–1273 K for 2 h, these alloy samples still

**Table 1**Data summary for the as-cast and heat-treated  $Al_{0.7}$ NiCoFe<sub>1.5</sub>Cr<sub>1.5</sub> HEA samples at different temperatures for 2 h, including the phase constitutions, volume fraction (f), lattice constant (a), lattice misfit ( $\varepsilon$ ) between BCC and B2 phases, and particle size (r) of B2 precipitates.

Alloy state	Phase constitution (f, %)	a (nm)	ε (%)	r (nm)
As-cast	BCC+ B2 (~ 49%)	$a_{BCC} = 0.2857 \pm 0.0001$ $a_{B2} = 0.2869 \pm 0.0002$	$0.42 \pm 0.04$	80 ± 20
673 K	BCC+ B2 (~ 53%)	$a_{BCC} = 0.2856 \pm 0.0001$ $a_{B2} = 0.2870 \pm 0.0003$	$0.49 \pm 0.05$	$90 \pm 15$
773 K	BCC+B2 (~ 57%)	$a_{BCC} = 0.2854 \pm 0.0002$ $a_{B2} = 0.2869 \pm 0.0003$	$0.52 \pm 0.07$	$100\pm10$
823 K	BCC + B2 (~ 52%) +σ (~ 10%)	$a_{BCC} = 0.2858 \pm 0.0002$ $a_{B2} = 0.2872 \pm 0.0002$	$0.49 \pm 0.06$	$105 \pm 15$
873 K	$BCC + B2 + \sigma (\sim 45\%)$	$a_{\sigma} = 0.8894 \pm 0.0006$ $c_{\sigma} = 0.4266 \pm 0.0008$	_	_
973 K	$BCC + B2 + \sigma + FCC$	_	_	_
1073 К	$BCC + B2 + \sigma + FCC$	$a_{\mathrm{BCC}} = 0.2865 \pm 0.0003$ $a_{\mathrm{B2}} = 0.2873 \pm 0.0002$ $a_{\sigma} = 0.8906 \pm 0.0007$ $c_{\sigma} = 0.4257 \pm 0.0005$ $a_{\mathrm{FCC}} = 0.3586 \pm 0.0003$	$0.28 \pm 0.10$	120 ± 15
1173 K	BCC + B2+FCC (~ 50%)	$a_{BCC} = 0.2867 \pm 0.0001$ $a_{B2} = 0.2873 \pm 0.0002$	$0.21 \pm 0.04$	$400\pm20$
1273 K	BCC + B2+FCC (~ 55%)	$a_{BCC} = 0.2868 \pm 0.0001$ $a_{B2} = 0.2872 \pm 0.0002$	$0.14 \pm 0.04$	$450 \pm 20$

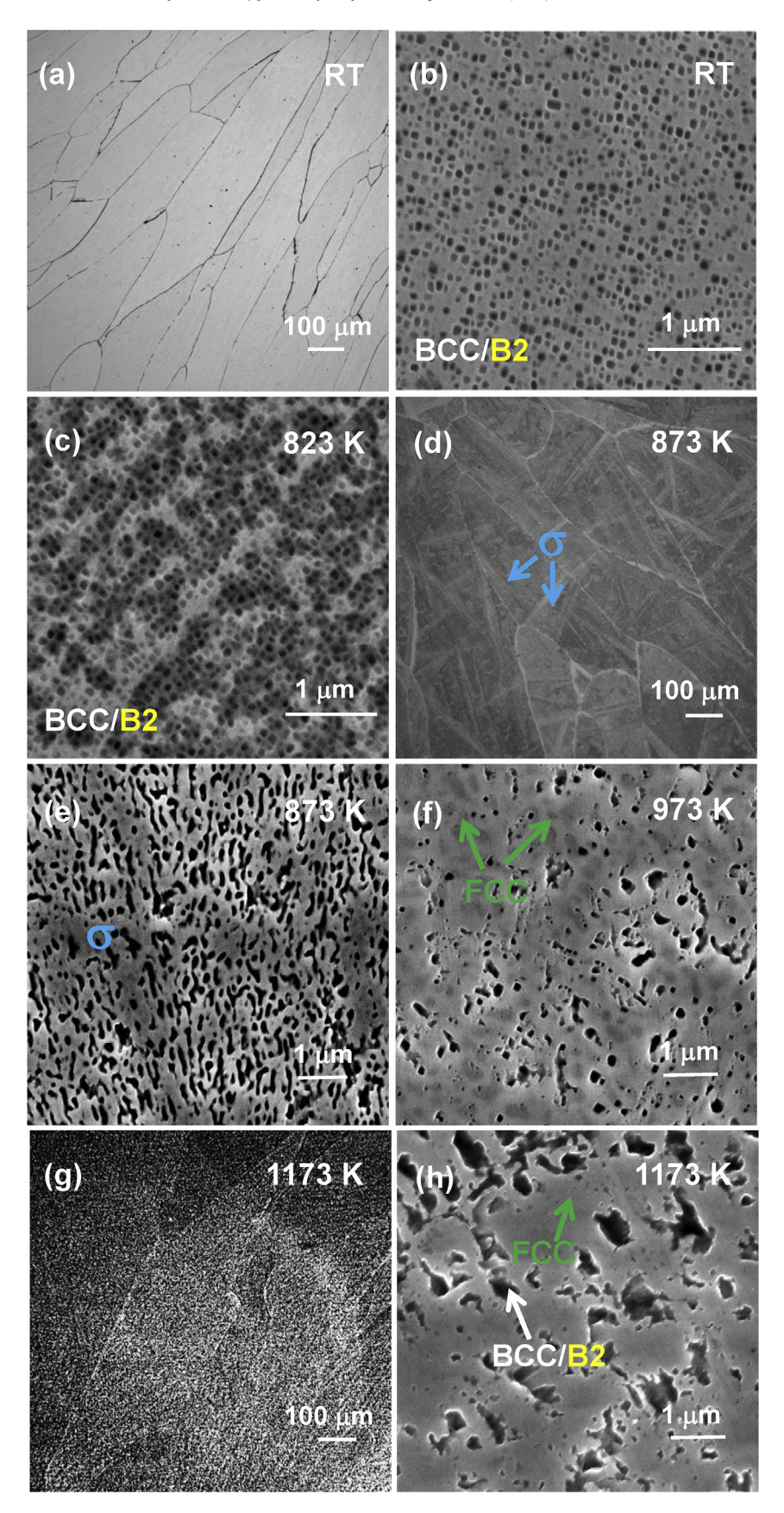


Fig. 2. OM and SEM micrographs of as-cast and heat-treated Al<sub>0.7</sub>NiCoFe<sub>1.5</sub>Cr<sub>1.5</sub> HEA samples at different temperatures for 2 h. (a, b): as-cast; (c): 823 K; (d, e): 873 K; (f): 973 K; (g, h): 1173 K. (a, d, g): OM images; (b, c, e, f, and h): SEM images.

maintain a coarse columnar-dendrite microstructure, as seen in Fig. 2(d, g). However, the microstructures in the inner-dendrites vary with increasing temperature. The coherent microstructure with cuboidal B2 nanoprecipitates in the BCC matrix can be stabilized up to 823 K (Fig. 2(c)). Further increasing temperature, the microstructure in the inner-dendrites will change sharply. A typical feature is that the B2 nanoprecipitates coarsened obviously, and the cuboidal shape is destroyed (Fig. 2(e, f, h)). In addition, the  $\sigma$  phase begins to appear at 823 K, and is dominant at 873 K, and then disappears after heat-treatment at 1173 K (Fig. 2(d, e, g, h)). Due to the redistribution of elements at HTs, the phase constitutions in the

heat-treated alloy samples will change gradually. The FCC phase appears at 973 K (Fig. 2(f)) and becomes dominant when heat-treated at 1173–1273 K, forming a dual-phase microstructure of (FCC + BCC/B2) (Fig. 2(h)). All of the phase structures will be identified carefully by TEM in the following.

In order to examine the coarsening behavior of cuboidal B2 nanoprecipitates with temperature, the TEM analysis was performed particularly. For the as-cast alloy, the dark-field (DF) image and the selected-area electron diffraction (SAED) pattern in Fig. 3(a and b) demonstrate that it is the cuboidal B2 nanoparticles with a size of r = 60-100 nm and with a volume fraction (f) of about 49%

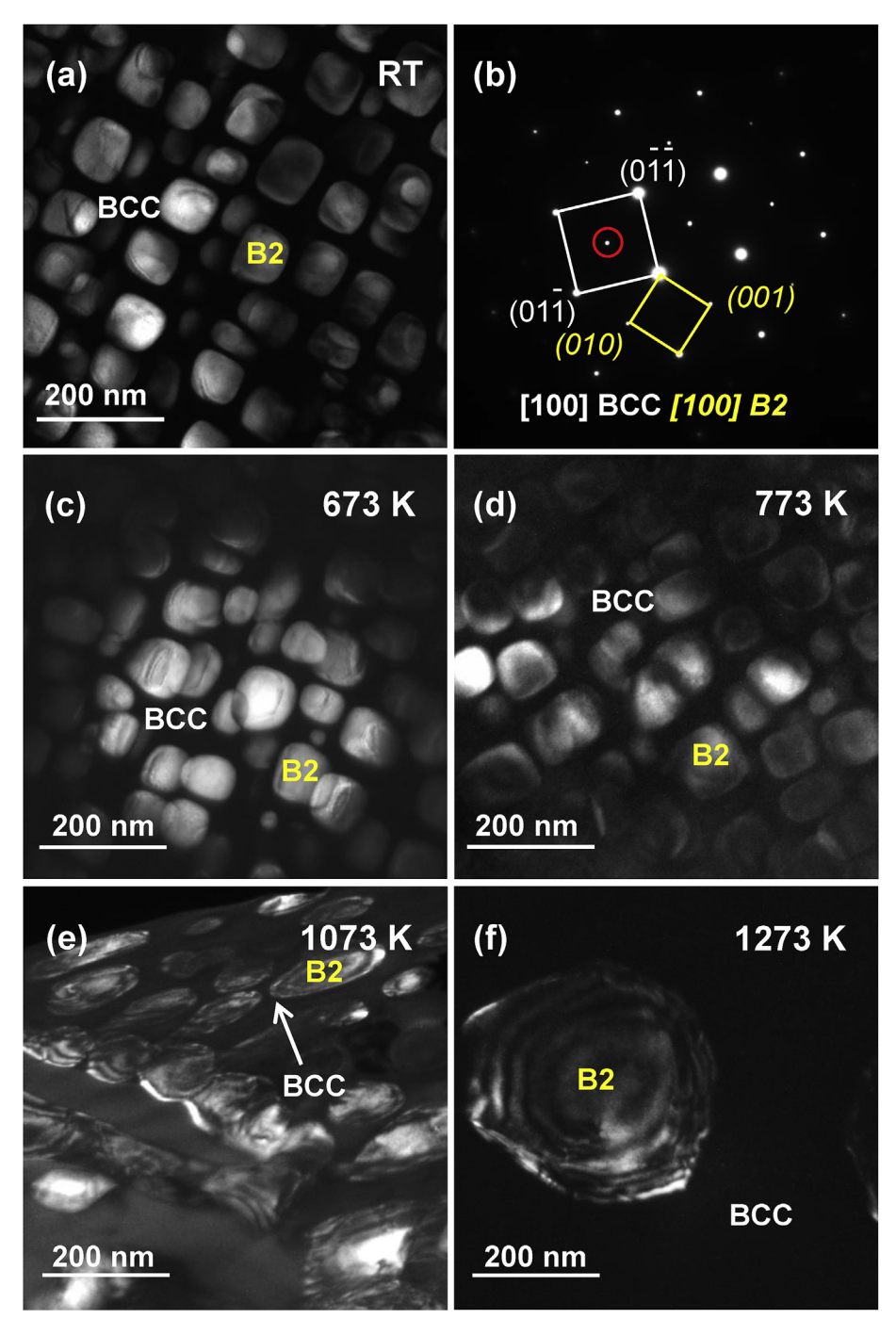


Fig. 3. TEM dark-field images and the corresponding SAED pattern of B2 nanoprecipitates in as-cast and heat-treated Al<sub>0.7</sub>NiCoFe<sub>1.5</sub>Cr<sub>1.5</sub> alloy samples at different temperatures for 2 h. (a, b): as-cast; (c): 673 K; (d): 773 K; (e): 1073 K; (f): 1273 K.

precipitated coherently in the BCC matrix. After heat treatments at 673–773 K for 2 h, the particle size of B2 cuboids increases slightly, being about r = 75-105 nm with f = 53% at 673 K (Fig. 3(c)) and r = 90 - 110 nm with f = 57% at 773 K (Fig. 3(d)), respectively. The B2nanoprecipitates are not coarsened at the 823 K treatment, similar to those at 773 K, while the volume fraction of B2 precipitates decreases to 52% due to the appearance of a small amount of the  $\sigma$ phase. When heat-treated at higher temperatures, it is found that the B2 particles are coarsened seriously and the particle shape tends to be irregular in the BCC/B2 region (Fig. 3(e and f)). Specifically, in the 1073 K-treated alloy sample, the B2 precipitates exhibit a ellipsoid-like shape, and the particle size increases up to r = 105-135 nm (Fig. 3(e)). Moreover, the B2 particle size can increase sharply with  $r = 430-470 \,\mathrm{nm}$  after the heat treatment at 1273 K, as presented in Fig. 3(f), which might result from the coalescence of B2 particles. Actually, the particle coalescence

phenomenon during coarsening has often been observed in Nibased superalloys at elevated temperatures [43–46].

The elemental distributions and compositional information in as-cast and heat-treated alloy samples at both 873 K and 1073 K were analyzed with the STEM. Fig. 4 shows the elemental distribution mapping in as-cast and 1073 K- treated alloy samples. It is found that the Al and Ni elements are enriched in the cuboidal nanoparticles (Fig. 4(b and c)). The measured chemical compositions of these precipitates are listed in Table 2, in which the amount of Al is much higher than the nominal value (12.5 at. %) and almost equal to that of Ni. For instance, the compositions of B2 precipitates in as-cast, 873 K- and 1073 K-treated alloy samples are Al<sub>30.2</sub>Ni<sub>32.1</sub>Co<sub>15.4</sub>Fe<sub>14.7</sub>Cr<sub>7.6</sub>, Al<sub>24.4</sub>Ni<sub>35.9</sub>Co<sub>15.7</sub>Fe<sub>17.3</sub>Cr<sub>6.7</sub>, and Al<sub>22.8</sub>Ni<sub>32.1</sub>Co<sub>15.9</sub>Fe<sub>18.4</sub>Cr<sub>10.8</sub> (at. %), respectively, which demonstrates that these precipitates exhibit a Ni/Al-rich B2 structure. It is also in consistence with the XRD results. In the as-cast state, Fe, Co,

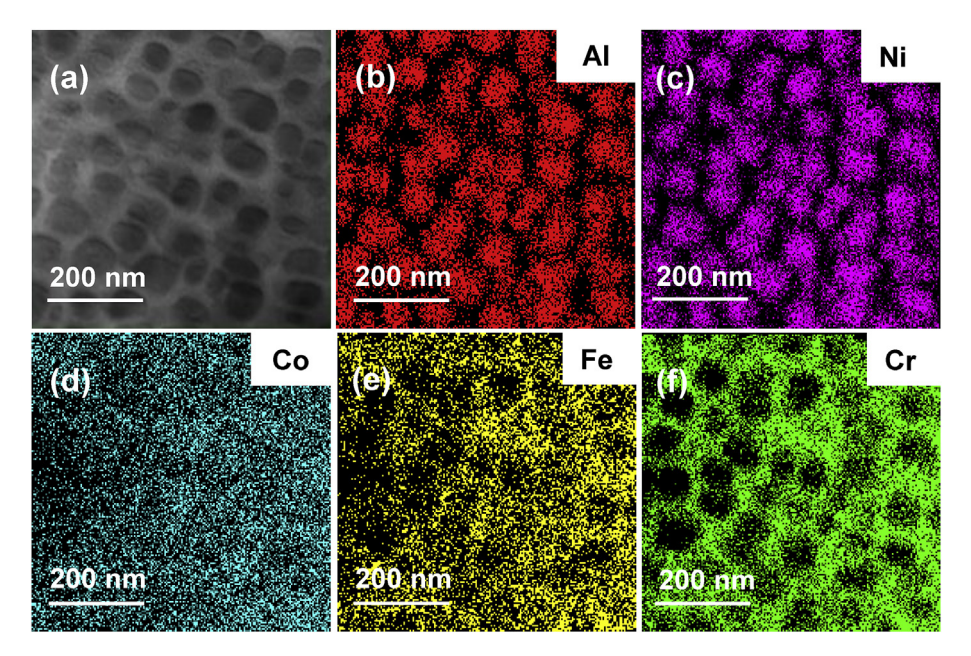


Fig. 4. Elemental distributions in as-cast Al<sub>0.7</sub>NiCoFe<sub>1.5</sub>Cr<sub>1.5</sub> HEA samples mapped with STEM.

**Table 2**Chemical compositions (atomic percent, at. %) of different phases in as-cast, 873 K-treated and 1073 K-treated HEA samples measured by STEM and CALPHAD. (The variations for the STEM results are represented by the standard deviation from the measured series.).

		Method	Chemical composition				
			Al	Ni	Со	Fe	Cr
Nominal composition of		12.50	17.50	17.50	26.25	26.25	
Al <sub>0.7</sub> NiCoF€		_					
as-cast	B2	Exp.	$30.2 \pm 0.6$	$32.1 \pm 0.7$	$15.4 \pm 0.7$	$14.7 \pm 0.8$	$7.6 \pm 0.9$
	BCC	Exp.	$2.6 \pm 0.7$	$6.2 \pm 0.8$	$16.2 \pm 0.9$	$29.2 \pm 0.8$	$45.8 \pm 0.9$
873 K	B2	Exp.	$24.4 \pm 0.6$	$35.9 \pm 0.8$	$15.7 \pm 1.0$	$17.3 \pm 1.2$	$6.7 \pm 0.8$
		Cal.	39.1	47.3	8.3	4.7	0.8
	BCC	Exp.	$3.1 \pm 0.5$	$11.4 \pm 0.8$	$20.3 \pm 0.7$	$28.6 \pm 1.1$	$36.6 \pm 0.6$
		CaÎ.	0.9	4.0	27.8	54.2	13.1
	σ	Exp.	$1.7 \pm 0.6$	$6.5 \pm 0.7$	$18.3 \pm 0.7$	$30.7 \pm 0.6$	$42.8 \pm 1.1$
		CaÎ.	0.1	4.3	19.5	29.4	46.8
1073 K	B2	Exp.	$22.8 \pm 0.7$	$32.1 \pm 0.8$	$15.9 \pm 0.7$	$18.4 \pm 0.6$	$10.8 \pm 0.7$
		Cal.	40.3	42.3	10.9	4.4	2.2
	BCC	Exp.	$4.5 \pm 0.8$	$13.0 \pm 1.0$	$18.5 \pm 0.8$	$26.0 \pm 0.7$	$38.0 \pm 0.8$
		Cal.	_	_	_	_	_
	σ	Exp.	$1.2 \pm 0.7$	$4.2 \pm 0.6$	$16.7 \pm 1.1$	$27.8 \pm 0.8$	$50.1 \pm 0.7$
		Cal.	0.5	4.0	17.6	30.5	47.4
	FCC	Exp.	$6.1 \pm 0.5$	$12.9 \pm 1.2$	$18.1 \pm 0.6$	$38.6 \pm 0.7$	$24.3 \pm 0.6$
		CaÎ.	2.9	12.1	22.3	38.2	24.5

Note: Exp. and Cal. in Method represent the experimental results and thermodynamic calculations, respectively.

and Cr are preferably segregated in the BCC matrix (Fig. 4(d, e, f)). With increasing the temperature, the total amount of Fe and Co is very close to that of Cr in some grains, which indicates that the matrix structure has transformed from BCC to a (Fe, Co) Cr-type  $\sigma$  phase. For example, the chemical composition of the  $\sigma$  phase in the 1073 K-treated alloy sample is Al<sub>1.2</sub>Ni<sub>4.2</sub>Co<sub>16.7</sub>Fe<sub>27.8</sub>Cr<sub>50.1</sub> (at. %), in which the total amount of 44.5 at. % of (Fe + Co) is very close to that of Cr content (50.1 at. %), and Al and Ni elements are scarce.

Moreover, to further verify that these B2 precipitates are coherent with the BCC matrix, the high-resolution TEM (HRTEM) images of the heat-treated alloy at 773 K along the [110] direction were displayed in Fig. 5, in which the interface between the BCC matrix and the cuboidal B2 nanoprecipitate is marked with a red curve (Fig. 5(a)). Fast Fourier transform (FFT) patterns derived from the precipitate and the matrix are shown in Fig. 5(b and c). An enlarged image (Fig. 5(d)) and its corresponding schematic illustration (Fig. 5(e)) reveal clearly the interfacial coherency between the BCC matrix and the B2 particle.

Besides the BCC and B2 phases, the phase structures in heat-treated alloy samples at HTs were also investigated, as seen in Fig. 6. After the heat treatment at 873 K, there exists a large amount of the  $\sigma$  phase, possessing a tetragonal structure (Fig. 6(a and b)). The appearance of  $\sigma$  resulted from the segregation of Fe and Cr elements in BCC regions, as seen in Fig. 4(k and l). In fact, the similar transformation from BCC to  $\sigma$  is common in Fe-Cr, Co-Cr, and Fe-Mo based alloys [33,45,46]. Then the amount of the  $\sigma$  phase will be

gradually reduced with further increasing temperature, and the FCC phase will appear due to the elemental redistributions at higher temperatures. As seen in Fig. 6(c ~ f), being the bright- and dark-field TEM images, as well as SAED patterns, the FCC,  $\sigma$ , and BCC/B2 phases coexisted in 1073 K-treated alloy. Moreover, the lattice constants of  $\sigma$  and FCC phases in heat-treated alloy samples at different temperatures are also listed in Table 1. This tendency is consistent with the existing thermodynamic calculations of the ascast BCC/B2 Al<sub>x</sub>NiCoFeCr HEA series (x = 0.7–1.6), in which the  $\sigma$  phase would appear first, and then the FCC solid-solution phase would coexist with the BCC/B2 phase at a high temperature range of 900–1473 K [16,47].

In order to further examine the stability of cuboidal B2 nano-precipitates in the 773 K-treated alloy, the heat treatment time was prolonged to 1080 h. Fig. 7 gives the morphologies of cuboidal B2 nanoprecipitates after the heat treatments for 2 h, 24 h, 216 h, 720 h, and 1080 h, respectively. It is found that these cuboidal B2 precipitates are still uniformly distributed in the BCC matrix, and the particle size remains unchanged even after being treated for 1080 h, as evidenced by the particle size values of  $r\!=\!85\!-\!105$  nm for the 720 h treatment and  $r\!=\!90\!-\!110$  nm for the 1080 h treatment (Fig. 7(e and f)). That is to say, the particle coarsening of B2 precipitates is difficult to occur at a temperature of  $T\!\leq\!773$  K, indicating that the cuboidal B2 precipitates can be stabilized to a high temperature of 773 K.

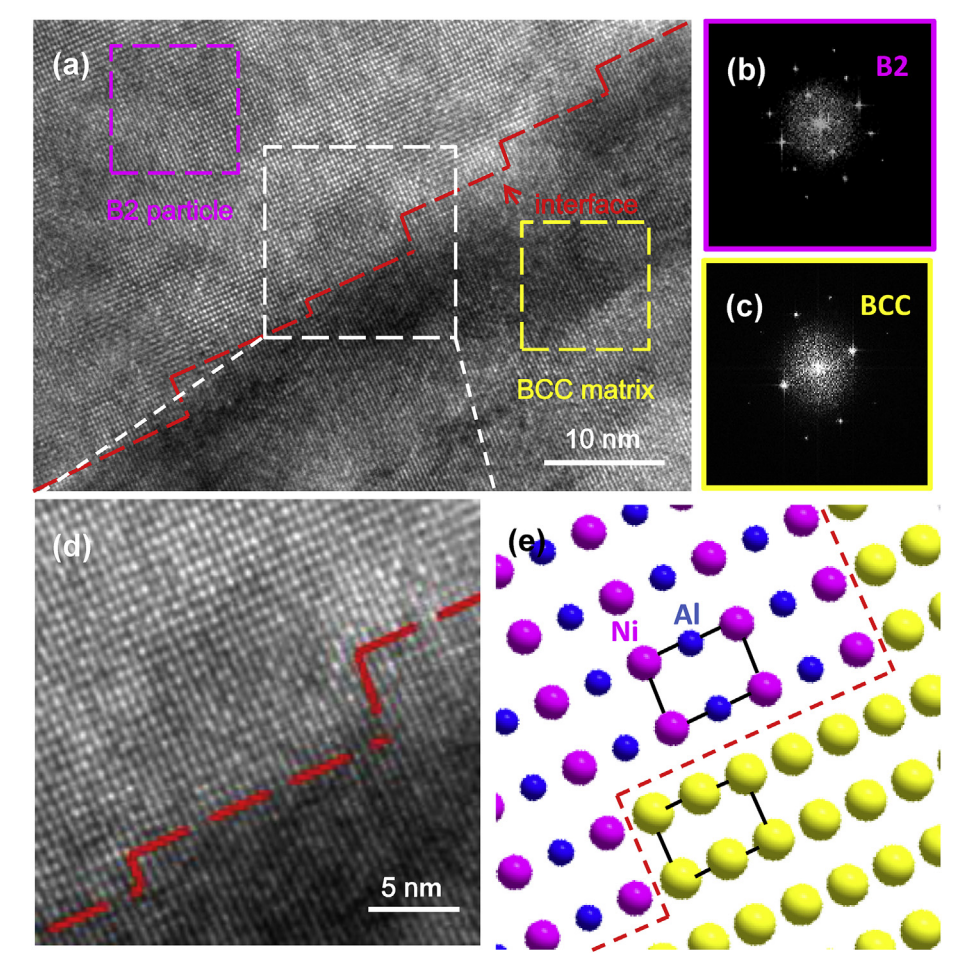


**Fig. 5.** HRTEM images of the heat-treated  $Al_{0.7}$ NiCoFe<sub>1.5</sub>Cr<sub>1.5</sub> HEA at 773 K for 2 h along the [110] direction. (a): HRTEM image showing the interfaces between the BCC matrix and cuboidal B2 nanoprecipitate; (b) and (c): FFT patterns of the BCC matrix and B2 nanoprecipitate, respectively; (d): a high-magnification HRTEM image from (a), showing details of the BCC/B2 interface; and (e): diagrammatic sketch of (d).

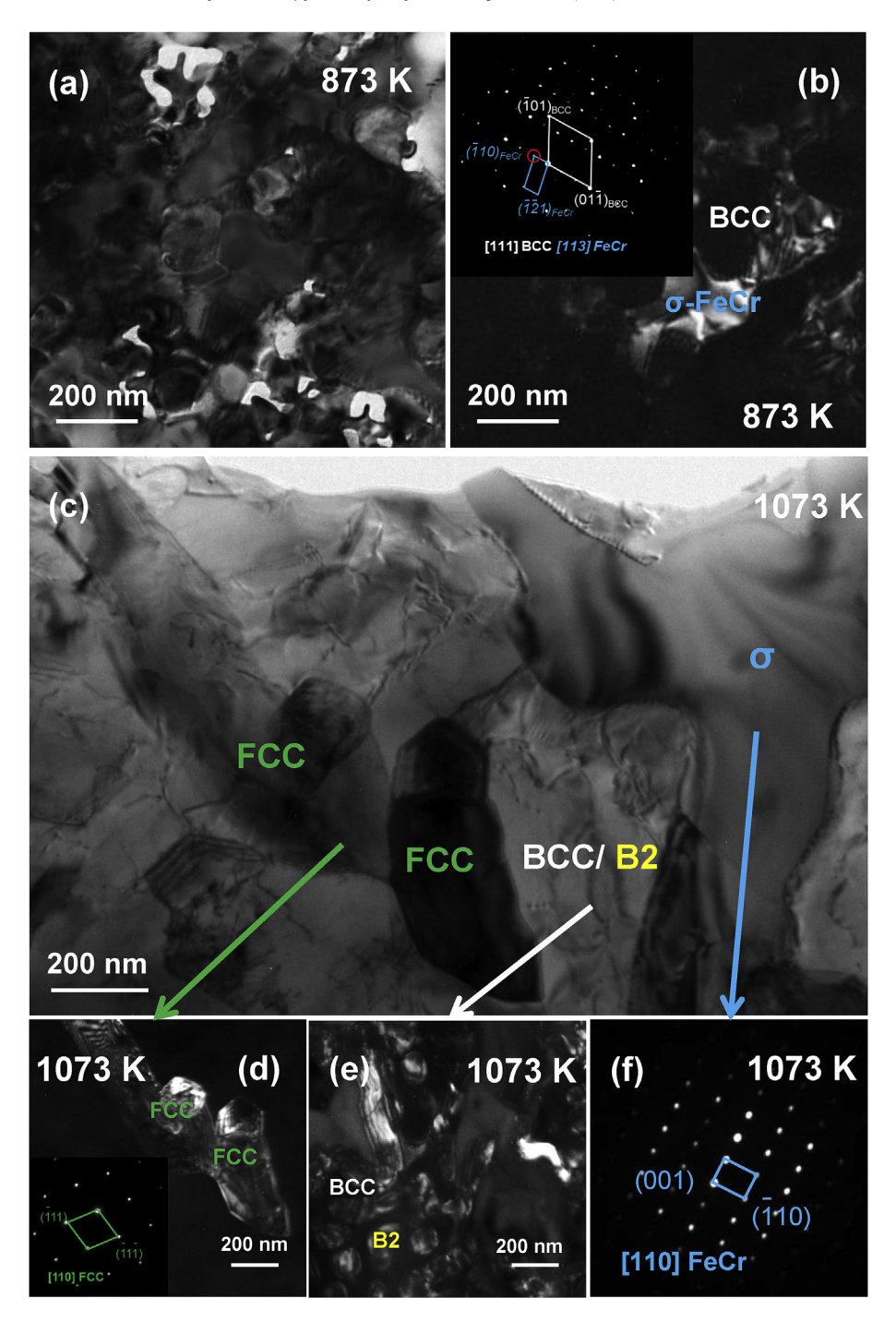
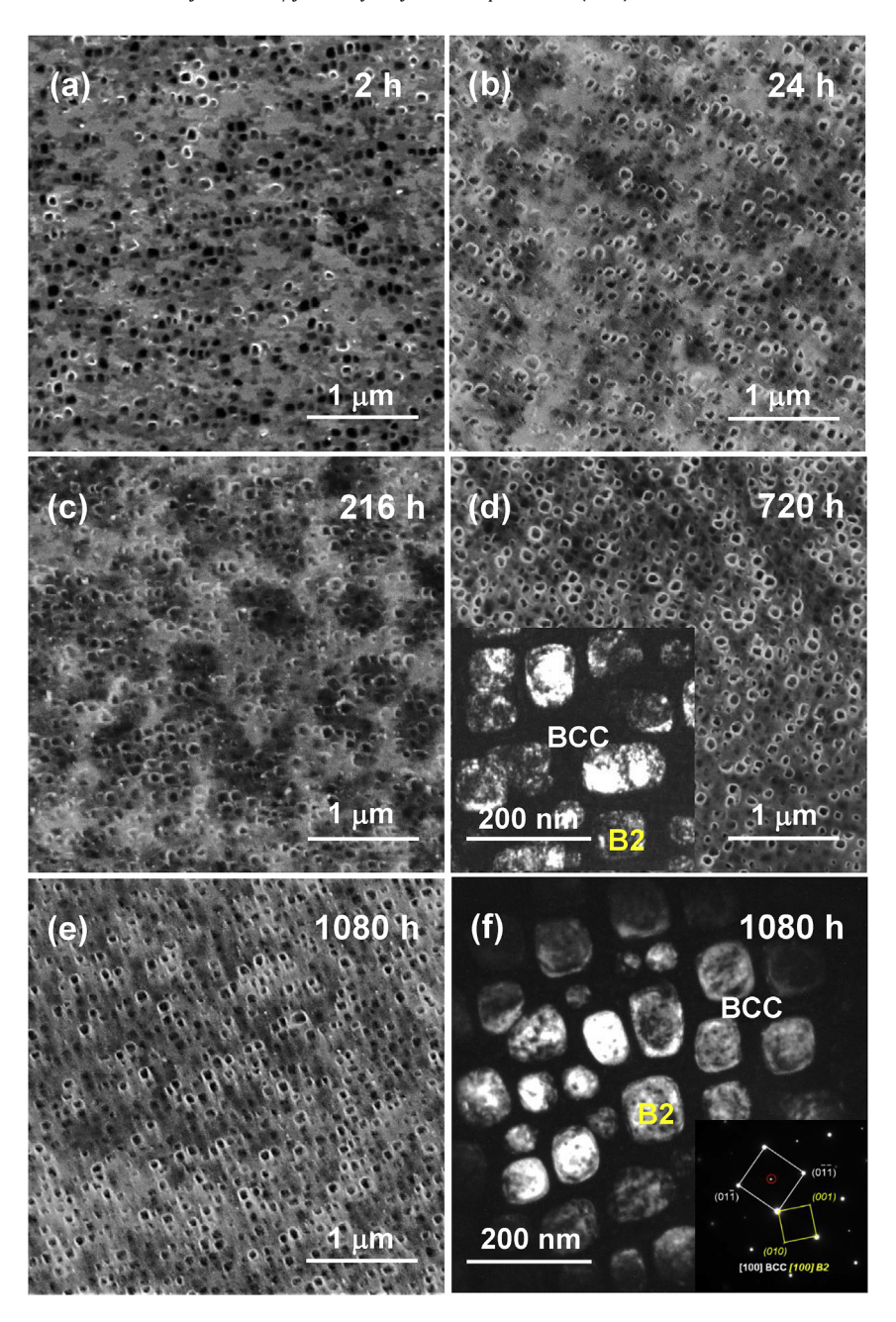


Fig. 6. TEM images and corresponding SAED patterns of different phases in heat-treated Al $_{0.7}$ NiCoFe $_{1.5}$ Cr $_{1.5}$  HEA samples at both 873 K (a ~ b) and 1073 K (c ~ f) for 2 h. (a, b): bright-field and dark-field images at 873 K; (c ~ f): bright-field image (c) and dark-field images and SAED patterns (d ~ f) of different phases (FCC, BCC/B2, and σ-FeCr) at 1073 K.

#### 3.2. Thermodynamic calculations

The CALPHAD approach in the design and development of HEAs has been well established to further understand their phase stability and microstructural evolution vs. chemistry and/or temperature [47–51]. For better understanding the experimental observations, the phase evolution of the Al<sub>0.7</sub>NiCoFe<sub>1.5</sub>Cr<sub>1.5</sub> HEA was calculated, as shown in Fig. 8(a). It can be seen that the melting temperature of this alloy is about 1605 K, and the primary phase during solidification is the BCC. Within the solid state, the ordered B2 phase is stable within the entire temperature range. The

disordered FCC phase is only stable at the temperature above 900 K. The calculated stable temperature range of the  $\sigma$  phase, which is originated from Cr-Fe and Co-Cr binary systems, is from 670 K to 1160 K. The disordered BCC phase coexists with both FCC and B2 phases at elevated temperatures above 1140 K and disappears with the formation of the  $\sigma$  phase. With further decreasing the temperature, the BCC phase forms again at about 927 K and its fraction continuously increases. At lower temperatures (T<700 K), the miscibility gap within the BCC phase starts to form, resulting in a phase decomposition of BCC #1 and BCC #2 phases. Furthermore, it is also noticed that a small amount of an ordered  $\gamma'$ -L12 phase is



 $\textbf{Fig. 7.} \hspace{0.5cm} \textbf{SEM} \hspace{0.5cm} \textbf{and} \hspace{0.5cm} \textbf{TEM} \hspace{0.5cm} \textbf{images} \hspace{0.5cm} \textbf{of} \hspace{0.5cm} \textbf{Al}_{0.7} \textbf{NiCoFe}_{1.5} \textbf{Cr}_{1.5} \hspace{0.5cm} \textbf{HEA} \hspace{0.5cm} \textbf{samples} \hspace{0.5cm} \textbf{after} \hspace{0.5cm} \textbf{heat} \hspace{0.5cm} \textbf{treatments} \hspace{0.5cm} \textbf{at} \hspace{0.5cm} \textbf{73} \hspace{0.5cm} \textbf{K} \hspace{0.5cm} \textbf{(a)}; \hspace{0.5cm} \textbf{24} \hspace{0.5cm} \textbf{h} \hspace{0.5cm} \textbf{(b)}; \hspace{0.5cm} \textbf{216} \hspace{0.5cm} \textbf{h} \hspace{0.5cm} \textbf{(d)}, \hspace{0.5cm} \textbf{and} \hspace{0.5cm} \textbf{1080} \hspace{0.5cm} \textbf{h} \hspace{0.5cm} \textbf{(e, f)}, \hspace{0.5cm} \textbf{respectively}.$ 

stable at a temperature below 770 K. From the equilibrium calculation of the Al $_{0.7}$ NiCoFe $_{1.5}$ Cr $_{1.5}$  HEA, not only the phase evolution with temperature can be obtained, but also the elemental distributions within each phase can be described. Fig.  $8(b \sim e)$  show the composition changes of B2, BCC, FCC, and  $\sigma$  phases with temperature, respectively. Besides, the chemical compositions (atomic percent, at. %) of different phases in 873 K-treated and 1073 K-treated HEA samples calculated by the CALPHAD approach are also listed in Table 2.

#### 3.3. Mechanical properties

The true compressive stress-strain curves of both as-cast and heat-treated alloy samples were tested at room temperature, as presented in Fig. 9, from which the compressive yield strength ( $\sigma_v$ )

was measured and listed in Table 3. The as-cast alloy sample exhibits a high strength with  $\sigma_y=1523$  MPa, which primarily resulted from the coherent microstructure with cuboidal B2 nanoprecipitates in the BCC matrix. Heat treatments at 673 K and 773 K for 2 h did not induce phase transformation, and the coherent microstructure with cuboidal B2 nanoprecipitation still remained in alloy samples. Thus, the heat-treated alloy samples exhibit a higher strength with  $\sigma_y=1686$  MPa at 673 K and  $\sigma_y=1928$  MPa at 773 K, respectively, which are much higher than that of the as-cast sample. It should be attributed to the particle size and volume fraction of B2 nanoprecipitates, which will be discussed in the following. The appearance of the brittle and hard  $\sigma$  phase at 823 K further enhances the strength ( $\sigma_y=2038$  MPa) of the alloy at the expense of the compression strain. When the  $\sigma$  phase is dominant at 873 K, the alloy sample is brittle, and the fracture happens before

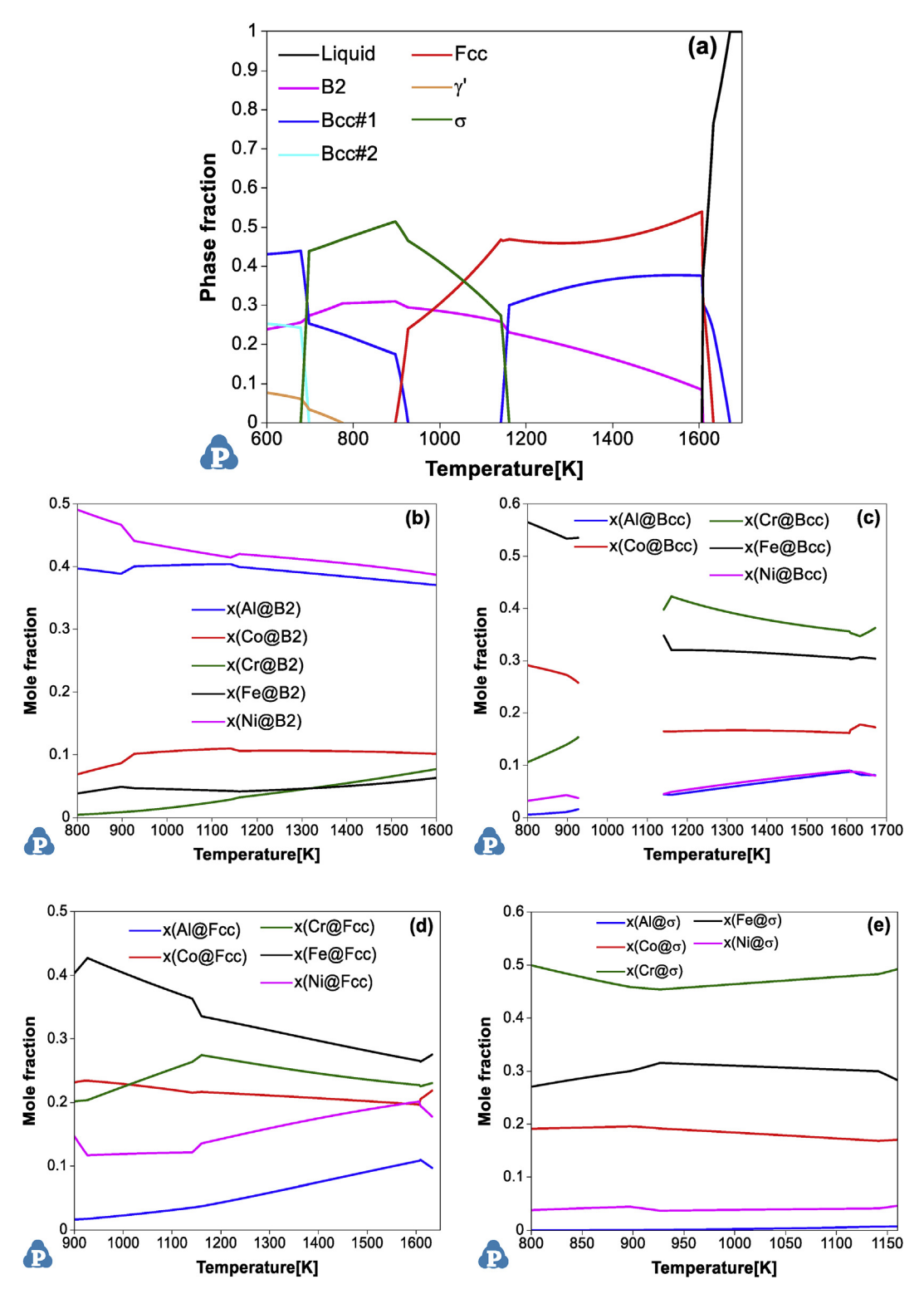
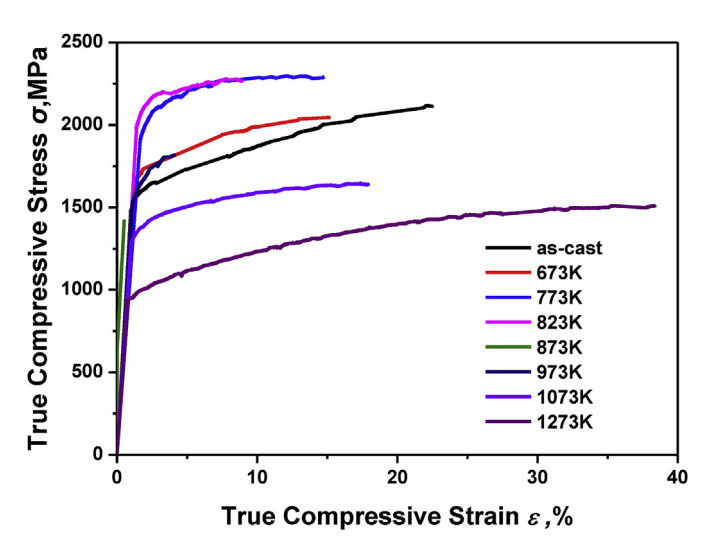


Fig. 8. CALPHAD diagram showing the relationships among the fractions (a) and composition changes (b~e) of various phases with temperatures for the Al<sub>0.7</sub>NiCoFe<sub>1.5</sub>Cr<sub>1.5</sub> HEA.

yielding. Further increasing temperature up to the range of 1073–1273 K, the strengths of heat-treated alloy samples decrease with  $\sigma_y = 941-1283$  MPa and the compressive strains increase, which resulted from the appearance of the soft FCC phase. In particular, the 1273 K-treated alloy shows an excellent mechanical property with a relatively higher strength ( $\sigma_y = 941$  MPa) and good

plasticity, in which no fracture occurs during the compressive test.

The results of microhardness measurements were also summarized in Table 3. The microhardness HV values of different-state alloy samples will vary with temperature due to the change of microstructures, following a similar tendency to that of  $\sigma_y$  with temperature, as seen in Fig. 10. The as-cast alloy has a high



**Fig. 9.** Room-temperature true compressive stress-strain curves of as-cast and heat-treated  $Al_{0.7}$ NiCoFe<sub>1.5</sub>Cr<sub>1.5</sub> HEA samples at different temperatures.

microhardness (HV=562) due to the special coherent microstructure of BCC and B2 phases. When the BCC phase transforms to the hard  $\sigma$  phase during heat treatments at HTs, the microhardness can be enhanced, up to the highest microhardness with HV=812 at 873 K. Then, the microhardness values of the heat-treated samples will decrease gradually with further increasing temperature, down to HV=334 at 1273 K since the FCC phase becomes dominant.

#### 4. Discussion

## 4.1. Understanding phase stability of the $Al_{0.7}NiCoFe_{1.5}Cr_{1.5}$ HEA via thermodynamic calculations

It can be seen that the observed as-cast microstructure of the Al<sub>0.7</sub>NiCoFe<sub>1.5</sub>Cr<sub>1.5</sub> HEA is composed of the major BCC phase, which is consistent with the thermodynamic prediction that the primary phase during the solidification is the BCC, as shown in Fig. 8(a). The experimental results indicate that the  $\sigma$  phase starts to be observed when heat-treated at 823 K and then disappears at the temperature above 1173 K, which shows a similar tendency to the calculated stable range of the  $\sigma$  (670–1140 K). In addition, the temperature range of experimentally-observed FCC phase is also close to the thermodynamic calculation. It should be pointed out that the discrepancies exist at low temperatures, as evidenced by the fact that the calculated phase decomposition of the BCC phase, the difference between the phase fractions of BCC and B2, and the appearance of the  $\gamma'$ -L1<sub>2</sub> phase were not found in experiments. The reason for such discrepancies is that the phase diagram represents the phase-equilibrium information, while the phase transformation in the solid state is the diffusion-controlled process, which always

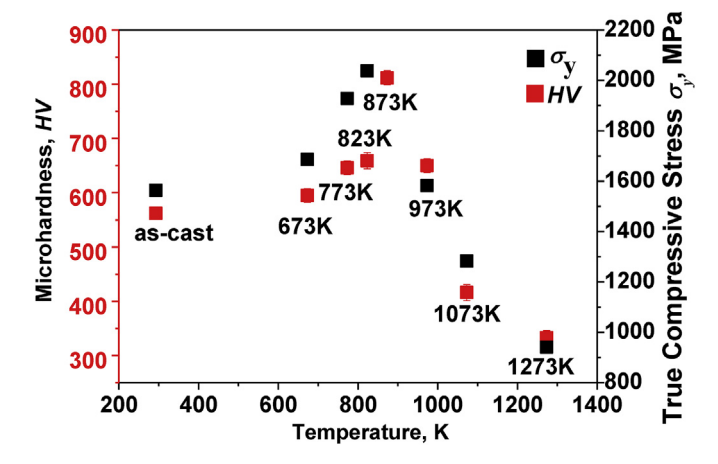


**Fig. 10.** Variations of compressive yield strength,  $\sigma$ , and microhardness, HV, of as-cast and heat-treated Al<sub>0.7</sub>NiCoFe<sub>1.5</sub>Cr<sub>1.5</sub> HEA samples at different temperatures.

takes much longer time to reach the equilibrium state. Actually, additional efforts should be used in the phase identification with the thermodynamic calculations, especially when there are two phases with similar crystal structures. It is also found that the major elements within the B2 phase are Al and Ni (Fig. 8(b)), which is similar to the STEM results (Fig. 4 and Table 2). The difference is that the calculated total amount (>80 at. %) of (Ni + Al) is relatively higher than the experimentally-measured value (~60 at. % in Table 2). The calculated Cr concentration in the  $\sigma$  phase is higher than that in BCC phase (Fig. 8(c, e)), which can be also identified well by the experimental data listed in Table 2 (compared these two phases at both 873 K and 1073 K). Moreover, the Cr, Fe, and Co are the major elements within the  $\sigma$  (Fig. 8(e) and Fig. 4(g ~ h)), which confirms the explanation that the  $\sigma$  phase is originated from the Cr-Fe and Cr-Co binary systems.

#### 4.2. Formation of cuboidal B2 nanoprecipitates

From both the SEM and TEM observations (Figs. 2 and 3), it can be found that the ordered B2 phase always coexisted with its parent BCC phase at different temperatures. Thus, the shape and size of B2 nanoprecipitates should vary with heat treatments at different temperatures.

It is well known that the equilibrium shape of precipitated particles is controlled by minimizing the total energy, including the elastic and interfacial energies of a system [52–54]. Since the elastic strain energy induced by the lattice mismatch at the interface between the precipitate and matrix is little in small-sized precipitates, the particle shape is primarily determined by minimizing the surface area of precipitates, which generally leads to the formation of spheroidal or ellipsoidal particles. With the precipitates growing up, the elastic-energy gradually takes over and

**Table 3**The L parameter (related to the shape of B2 precipitates), compressive yield strength ( $\sigma_y$ ), and microhardness (HV) of the as-cast and heat-treated Al<sub>0.7</sub>NiCoFe<sub>1.5</sub>Cr<sub>1.5</sub> HEA samples at different temperatures for 2 h.

Alloy state	as-cast	673 K	773 K	823 K	873 K	973 K	1073 K	1273 K
$L(10^{-1})$ $\sigma_{y}$ (MPa) $HV$	1.47	2.25	2.81	2.50	-	-	0.98	0.92
	1523	1686	1928	2038	-	1583	1283	941
	562 ± 10	595 ± 13	646 ± 12	659 ± 15	812 ± 13	650 ± 9	416 ± 15	334 ± 13

Note: the *L* parameter values are derived from the equation of  $L = \frac{\varepsilon^2 C_{44} r}{s}$  [54]

becomes dominant. The relative contributions of the elastic and interfacial energies to the total energy can be quantified using the L parameter [54], defined as:

$$L = \frac{\varepsilon^2 C_{44} r}{s} \tag{1}$$

where  $\varepsilon$  is the lattice misfit,  $C_{44}$  is the elastic constant of the matrix, r is the average precipitate size, and s is the average specific interfacial energy. In this study, the lattice misfit,  $\varepsilon$ , between BCC and B2 phases is calculated, using the equation of  $\varepsilon = 2 \times (a_{B2} - a_{B2} + a_{B$  $a_{\rm BCC})/(a_{\rm B2}+a_{\rm BCC})$ , where  $a_{\rm B2}$  and  $a_{\rm BCC}$  are the lattice constants of B2 and BCC phases, respectively. The  $C_{44}$  and s values for BCC/B2 alloys are taken from those of the B2-NiAl phase, being  $C_{44} = 130 \,\text{GPa}$  and  $s = 0.125 \,\text{J/m}^2 \,[54-57]$ . Thus, we can quantitatively estimate the L values in as-cast and heat-treated samples at different temperatures according to Eq. (1), which are listed in Table 3. The involved parameters for the calculation, including lattice constants (a) of BCC and B2 phases, lattice misfit,  $\varepsilon$ , between BCC and B2 phases, the particle size, r, of B2 precipitates in alloy samples were summarized in Table 1. It is due to the moderate L of 1.47 in the as-cast state, which favors the formation of coherent cuboidal B2 precipitates. After heat treatments at 673 K and 773 K, although samples have a relatively-high L value, being 2.25 and 2.81, respectively, the coherent microstructure with cuboidal B2 nanoprecipitates can still be maintained (Fig. 3(c and d)). By contrast, the disappearance of cuboidal B2 precipitates (with an ellipsoidal shape) in heat-treated samples at both 1073 K and 1273 K (Fig. 3(e and f)) might result from a relatively-lower L value, being 0.98 and 0.92, respectively. Since the particle sizes of B2 nanoprecipitates in as-cast and heat-treated samples are comparable, the lattice misfit,  $\varepsilon$ , must play the key role in determining the shape of these B2 particles. Therefore, it is due to the moderate lattice misfit that the cuboidal B2 nanoprecipitates can be maintained in the as-cast and heat-treated alloy samples at T < 823 K. The ellipsoidal shape of precipitates in heat-treated samples at a higher temperature of 1073-1273 K is a result of a small lattice misfit of  $\varepsilon = 0.14 - 0.28\%$ .

### 4.3. Precipitation strengthening of coherent cuboidal B2 precipitates

In our previous work, it was found that the high strength caused by the coherent microstructure with cubolidal B2 nanoprecipitates in the BCC matrix of HEAs is mainly dependent on the coherent precipitation strengthening [38]. The mechanism for precipitation strengthening can be divided into two categories, Orowan bypassing, which occurs when the particles are large or incoherent with the matrix, and particle shearing, which dominates when the precipitates are coherent and small. Since the shearing and bypassing mechanisms occur concurrently and are independent of each other, the strengthening is determined by the smaller increment of shearing or bypassing. Specially, for the shearing mechanism, three factors contribute to the increase in the yield strength, coherency strengthening ( $\Delta \sigma_{CS}$ ), modulus-mismatch strengthening  $(\Delta \sigma_{\rm MS})$ , and order strengthening  $(\Delta \sigma_{\rm OS})$ . It should be noticed that these strengthening processes are sequential, the former two ( $\Delta \sigma_{\rm CS}$ and  $\Delta \sigma_{\rm MS}$ ) occur prior to the shearing of precipitates by dislocations, and the latter one ( $\Delta \sigma_{OS}$ ) during the shearing. In this case, the larger of ( $\Delta\sigma_{\rm CS}$  +  $\Delta\sigma_{\rm MS}$ ) or  $\Delta\sigma_{\rm OS}$  would be the total strength increment from the shearing mechanism.

The equations available to calculate these strength increments are [58-67]:

$$\Delta \sigma \text{CS} = M^* \alpha \varepsilon^* (G \varepsilon c)^{3/2} * (rf/0.5Gb)^{1/2}$$
 (2)

$$\Delta \sigma MS = M*0.0055*(\Delta G)^{\frac{1}{2}*} \left(\frac{r}{b}\right)^{\frac{3m}{2}-1}$$
 (3)

$$\Delta \sigma OS = M*0.81*\frac{\gamma apb}{2b}*\left(\frac{3\pi f}{8}\right)^{\frac{1}{2}}$$
 (4)

$$\Delta \sigma \text{orowan} = M * \frac{0.4Gb}{\pi \sqrt{1 - \nu}} * \frac{\ln\left(2\sqrt{\frac{2}{3}}r/b\right)}{\lambda p}$$
 (5)

$$\lambda p = 2\sqrt{\frac{2}{3}}r\left(\sqrt{\frac{\pi}{4f}} - 1\right) \tag{6}$$

where M=2.73 for the BCC structure (Taylor Factor) [59],  $\alpha_{\varepsilon}=2.6$  (a constant) [60,61], m=0.85 (a constant) [61,62], G and  $\Delta G$  are the shear modulus of the matrix and the shear-modulus mismatch between the precipitates and matrix, respectively;  $\varepsilon_{\rm C}=2\varepsilon/3$  is the constrained lattice misfit [59–61], r is the average particle size, f is the volume fraction of precipitates, b is the Burgers vector, v is the Poisson ratio (v=0.3 for BCC HEAs [67]),  $\gamma_{\rm apb}$  is the anti-phase boundary energy of precipitates, and  $\lambda_{\rm p}$  is the inter-precipitate spacing.

According to these equations and the parameters, the strength increments of  $\Delta\sigma_{\rm CS}$ ,  $\Delta\sigma_{\rm MS}$ ,  $\Delta\sigma_{\rm OS}$ , and  $\Delta\sigma_{\rm orowan}$  of the as-cast Al<sub>0.7</sub>NiCoFe<sub>1.5</sub>Cr<sub>1.5</sub> HEA are calculated, being  $\Delta\sigma_{\rm CS}=1549$  MPa,  $\Delta\sigma_{\rm MS}=41$  MPa,  $\Delta\sigma_{\rm OS}=849$  MPa, and  $\Delta\sigma_{\rm orowan}=1553$  MPa. Parameters used for calculations are G=83 GPa (for  $\alpha$ -Fe) [68], the Burgers vector  $b=\sqrt{3}\times a_{\rm BCC}/2=0.2474$  nm, r=80 nm, f=0.49,  $\Delta G=83-80=3$  GPa (the shear modulus of B2-NiAl is G=80 GPa [55]), and  $\gamma_{\rm apb}=0.25$  J/m² [56], respectively. The strength increment,  $\Delta\sigma_{\rm OS}$ , from the order strengthening is noted to be less than ( $\Delta\sigma_{\rm CS}+\Delta\sigma_{\rm MS}$ ) from coherency strengthening and modulus mismatch strengthening, suggesting the coherency strengthening dominates.

Since the dominant role of shearing strengthening or bypassing strengthening is dependent on the smaller of  $(\Delta\sigma_{\text{CS}} + \Delta\sigma_{\text{MS}})$  or  $\Delta\sigma_{\text{orowan}}$ , the variations of strength increments of  $(\Delta\sigma_{\text{CS}} + \Delta\sigma_{\text{MS}})$ 

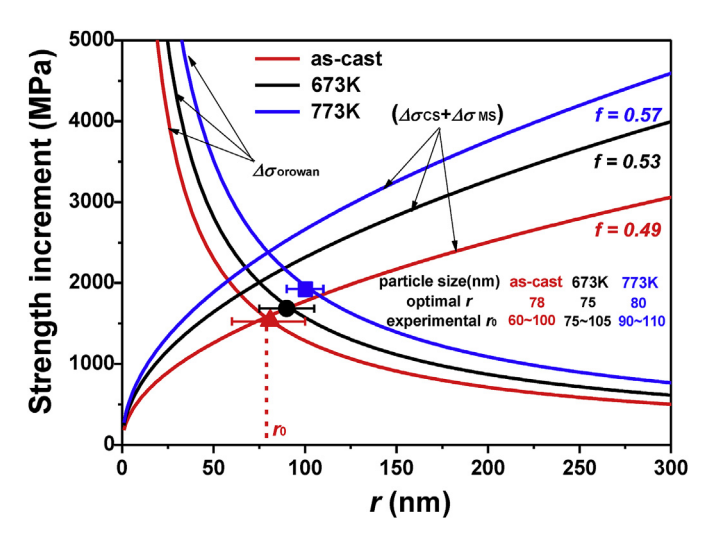


**Fig. 11.** Computations of  $(\varDelta\sigma_{\text{CS}} + \varDelta\sigma_{\text{MS}})$  and  $\varDelta\sigma_{\text{orowan}}$  as a function of particle size, r, in as-cast, 673 K-treated, and 773 K-treated HEA samples. The optimal particle sizes  $(r_0)$  and the experimentally-measured values (r) are also marked for each sample.

and  $\Delta \sigma_{\text{orowan}}$  are plotted as a function of the particle size, r, for the as-cast, 673 K-, and 773 K-treated HEA samples, in which the volume franction f is fixed, as shown in Fig. 11. Ideally, the largest yield increment could reached strength be  $(\Delta\sigma_{\rm CS}+\Delta\sigma_{\rm MS})=\Delta\sigma_{\rm orowan}$  at an optimal particle size,  $r_0$ , with a fixed f. Thereof, the calculated optimal size of cuboidal B2 precipitates is  $r_0 = 78$  nm in the as-cast alloy,  $r_0 = 75$  nm in the 673 K-treated alloy, and  $r_0 = 80$  nm in 773 K-treated alloy, respectively. It is of interest to emphasize that the theoretically-predicted  $r_0$  values in these three states are comparable, which is attributed primarily to the fact that the lattice misfit  $\varepsilon$  values of BCC and B2 phases in these three states are almost equal. What's more, the experimental average value of r = 80 nm of B2 cuboids in the as-cast state is nearly equal to the theoretically optimal size ( $r_0 = 78 \text{ nm}$ ), indicating that the maximum increment in the yield strength can be reached. After heat treatments at 673–773 K for 2 h, the B2 particle size increases slightly and is larger than the optimal value,  $r_0$ , which means that the experimental yield strength cannot reach the theoretically maximum value. However, the heat-treated alloys still possess a higher strength since the particle size just exceeds the optimal value, in which the Orowan bypassing strengthening mechanism is dominant. For instance, in the 773 K-treated HEA, the ideally maximum yield strength increment is  $\Delta \sigma = 2375 \,\text{MPa}$  with  $r_0 = 80$  nm, while the experimental compressive yield strength is  $\sigma_{\rm V}$  = 1928 MPa, slightly lower than the theoretical value.

#### 5. Conclusions

In this study, the formation of cuboidal B2 nanoprecipitates in the BCC Al<sub>0.7</sub>NiCoFe<sub>1.5</sub>Cr<sub>1.5</sub> HEA and the microstructural evolution with temperature have been investigated from the viewpoints of both experiments and thermodynamic calculations. The coherent microstructure with cuboidal B2 nanoprecipitates in the BCC matrix can be formed in the as-cast state, which can still be maintained when heat-treated at a high temperature of 823 K for 2 h with a particle size of 60–120 nm. Even after the heat treatment at 773 K for 1080 h, the cuboidal B2 nanoprecipitates still stabilized without any coarsening, showing a good microstructural stability with cuboidal B2 precipitation. It is due to a moderate lattice misfit ( $\varepsilon = 0.4 - 0.5\%$ ) that favors the formation of coherent cuboidal B2 nanoprecipitates with an appropriate partile size of 60-120 nm, which finally results in a higher strength with  $\sigma_V = 1500-1900$  MPa in light of the coherent precipitation mechanism. With increasing the temperature, the cuboidal B2 nanoprecipitates could be coarsened with the change of the particle shape. In addition, the Fe/ Cr-rich  $\sigma$  phase appears after the heat treatment at 873 K and can be present until a higher temperature of 1173 K, leading to brittleness with an increased microhardness (the highest HV = 812after the treatment at 873 K). The FCC phase appears after the heat treatment at 973 K and becomes dominant gradually above 1173 K, which can soften the alloy (the lowest  $\sigma_V = 941$  MPa and HV = 334after the treatment at 1273 K). Moreover, the thermodynamic calculations show a similar tendency to the experimental results, which can provide a better understanding of the microstructural evolution of HEAs.

#### Acknowledgements

It was supported by the National Key Research and Development Plan (2017YFB0702400), the Science Challenge Project (TZ2016004), the National Magnetic Confinement Fusion Energy Research Project (2015GB121004), the International Science & Technology Cooperation Program of China (2015DFR60370), and the National Natural Science Foundation of China [No. U1610256]. P.K. Liaw would like to acknowledge the U.S. Army Research Office

project (W911NF-13-1-0438), and the National Science Foundation of U.S. (DMR-1611180 and 1809640).

#### References

- J.W. Yeh, S.K. Chen, S.J. Lin, J.Y. Gan, T.S. Chin, T.T. Shun, C.H. Tsau, S.Y. Chang, Nanostructured high-entropy alloys with multiple principal elements: novel alloy design concepts and outcomes, Adv. Eng. Mater. 6 (2004) 299–303.
- [2] O.N. Senkov, J.D. Miller, D.B. Miracle, C. Woodward, Accelerated exploration of multi-principal element alloys with solid solution phases, Nat. Commun. 6 (2015) 6529.
- [3] Y.F. Ye, Q. Wang, J. Lu, C.T. Liu, Y. Yang, High-entropy alloy: challenges and prospects, Mater. Today 19 (2016) 349–362.
- [4] D.B. Miracle, O.N. Senkov, A critical review of high entropy alloys and related concepts, Acta Mater. 122 (2016) 448–511.
- [5] S.J. Sun, Y.Z. Tian, H.R. Lin, X.G. Dong, Y.H. Wang, Z.J. Zhang, Enhanced strength and ductility of bulk CoCrFeMnNi high entropy alloy having fully recrystallized ultrafine-grained structure, Mater. Des. 133 (2017) 122–127.
- [6] S.L. Wei, F. He, C.C. Tasan, Metastability in high-entropy alloys: a review, J. Mater. Res. 33 (2018) 2924–2937.
- [7] Z.Y. Lyu, X.S. Fan, C. Lee, S.Y. Wang, R. Feng, P.K. Liaw, Fundamental understanding of mechanical behavior of high-entropy alloys at low temperatures: a review, J. Mater. Res. 33 (2018) 2998–3010.
- [8] Y. Zou, Nanomechanical studies of high-entropy alloys, J. Mater. Res. 33 (2018) 3035–3054.
- [9] M.A. Hemphill, T. Yuan, G.Y. Wang, J.W. Yeh, C.W. Tsai, A. Chuang, P.K. Liaw, Fatigue behavior of Al<sub>0.5</sub>CoCrCuFeNi high entropy alloys, Acta Mater. 60 (2012) 5723–5734.
- [10] Z. Tang, T. Yuan, C.W. Tsai, J.W. Yeh, C.D. Lundin, P.K. Liaw, Fatigue behavior of a wrought Al<sub>0.5</sub>CoCrCuFeNi two-phase high-entropy alloy, Acta Mater. 99 (2015) 247–258.
- [11] M. Seifi, D. Li, Z. Yong, P.K. Liaw, J.J. Lewandowski, Fracture toughness and fatigue crack growth behavior of as-cast high-entropy alloys, JOM 67 (2015) 2288–2295.
- [12] W.D. Li, G. Wang, S.W. Wu, P.K. Liaw, Creep, fatigue, and fracture behavior of high-entropy alloys, J. Mater. Res. 33 (2018) 3011–3034.
- [13] Y. Zhang, T.T. Zuo, Z. Tang, M.C. Gao, K.A. Dahmen, P.K. Liaw, Z.P. Lu, Microstructures and properties of high-entropy alloys, Prog. Mater. Sci. 61 (2014) 1—93
- [14] Y. Zhang, Y.J. Zhou, J.P. Lin, G. Chen, P.K. Liaw, Solid-solution phase formation rules for multi-component alloys, Adv. Eng. Mater. 10 (2008) 534–538.
- [15] B. Gludovatz, A. Hohenwarter, D. Catoor, E.H. Chang, E.P. George, R.O. Ritchie, A fracture-resistant high-entropy alloy for cryogenic applications, Science 345 (2014) 1153.
- [16] Y.F. Kao, T.J. Chen, S.K. Chen, J.W. Yeh, Microstructure and mechanical property of as-cast, -homogenized, and -deformed Al $_x$ CoCrFeNi (0 $\leq$ x $\leq$ 2) high entropy alloys, J. Alloys Compd. 488 (2009) 57–64.
- [17] Y.P. Wang, B.S. Li, M.X. Ren, C. Yang, H.Z. Fu, Microstructure and compressive properties of AlCrFeCoNi high entropy alloy, Mater. Sci. Eng. 491 (2008) 154–158.
- [18] Y. Ma, B.B. Jiang, C.L. Li, Q. Wang, C. Dong, P.K. Liaw, F. Xu, L. Sun, The BCC/B2 morphologies in  $Al_x$ NiCoFeCr high-entropy alloys, Metals 7 (2017) 57.
- [19] T.T. Shun, Y.C. Du, Microstructure and tensile behaviors of FCC Al<sub>0.3</sub>CoCrFeNi high entropy alloy, J. Alloys Compd. 479 (2009) 157–160.
- [20] J.C. Rao, V. Ocelík, D. Vainchtein, Z. Tang, P.K. Liaw, J.ThM. De Hosson, The fcc-bcc crystallographic orientation relationship in AlxCoCrFeNi high-entropy alloys, Mater. Lett. 176 (2016) 29–32.
- [21] J.C. Rao, V. Ocelík, D. Vainchtein, Z. Tang, P.K. Liaw, J.ThM. De Hosson, On the onset of nano-ordered phase distributions in high-entropy alloys, Rev. Adv. Mater. Sci. 48 (2017) 105–111.
- [22] P. Caron, T. Khan, Evolution of Ni-based superalloys for single crystal gas turbine blade applications, Aerosol Sci. Technol. 3 (1999) 513–523.
- [23] J.V. Goerler, I. Lopez-Galilea, L.M. Roncery, O. Shchyglo, W. Theisen, I. Steinbachet, Topological phase inversion after long-term thermal exposure of nickel-base superalloys: experiment and phase-field simulation, Acta Mater. 124 (2017) 151–158.
- [24] Y.Y. Zhao, H.W. Chen, Z.P. Lu, T.G. Nieh, Thermal stability and coarsening of coherent particles in a precipitation-hardened (NiCoFeCr)<sub>94</sub>Ti<sub>2</sub>Al<sub>4</sub>, highentropy alloy, Acta Mater. 147 (2018) 184–194.
- [25] O.N. Senkov, G.B. Wilks, J.M. Scott, D.B. Miracle, Mechanical properties of Nb<sub>25</sub>Mo<sub>25</sub>Ta<sub>25</sub>W<sub>25</sub> and V<sub>20</sub>Nb<sub>20</sub>Mo<sub>20</sub>Ta<sub>20</sub>W<sub>20</sub> refractory high entropy alloys, Intermetallics 19 (2011) 698–706.
- [26] O.N. Senkov, J.M. Scott, S.V. Senkova, D.B. Miracle, C.F. Woodward, Microstructure and room temperature properties of a high-entropy TaNbHfZrTi alloy, J. Alloys Compd. 509 (2011) 6043–6048.
- [27] O.N. Senkov, S.V. Senkova, C. Woodward, Effect of aluminum on the microstructure and properties of two refractory high-entropy alloys, Acta Mater. 68 (2014) 214–228.
- [28] O.N. Senkov, D.B. Miracle, K.J. Chaput, J. Couzinie, Development and exploration of refractory high entropy alloys—a review, J. Mater. Res. 33 (2018) 3092–3128.
- [29] V.S. Soni, B. Gwalani, O.N. Senkov, B. Viswanathan, T. Alam, D.B. Miracle, R. Banerjee, Phase stability as a function of temperature in a refractory high-

- entropy alloy, J. Mater. Res. 33 (2018) 3235-3246.
- [30] F. Otto, A. Dlouhy, C. Somsen, H. Bei, G. Eggeler, E.P. George, The influences of temperature and microstructure on the tensile properties of a CoCrFeMnNi high-entropy alloy, Acta Mater. 61 (2013) 5743-5755.
- [31] N.D. Stepanov, D.G. Shaysultanov, M.S. Ozerov, S.V. Zherebtsov, G.A. Salishchev, Second phase formation in the CoCrFeNiMn high entropy alloy after recrystallization annealing, Mater. Lett. 185 (2016) 1-4.
- [32] A. Munitz, S. Salhov, S. Hayun, N. Frage, Heat treatment impacts the microstructure and mechanical properties of AlCoCrFeNi high entropy alloy, J. Alloys Compd. 683 (2016) 221–230.
- W.R. Wang, W.L. Wang, J.W. Yeh, Phases, microstructure and mechanical properties of Al<sub>x</sub>CoCrFeNi high-entropy alloys at elevated temperatures, . Alloys Compd. 589 (2014) 143–152.
- [34] M. Hillert, in: H.J. Aaronson (Ed.), Phase Transformations, ASM, Metals Park, OH, 1970.
- [35] L. Kaufman, H. Bernstein, Computer Calculation of Phase Diagrams, Academic Press New York 1970
- [36] Y.A. Chang, S. Chen, F. Zhang, X. Yan, F. Xie, R. Schmid-Fetzer, W.A. Oates, Phase diagram calculation: past, present and future, Prog. Mater. Sci. 49 (2004) 313-345.
- J.C. Rao, H.Y. Diao, V. Ocelík, D. Vainchtein, C. Zhang, C. Kuo, Z. Tang, W. Guo, J.D. Poplawsky, Y. Zhou, P.K. Liaw, J.ThM. De Hosson, Secondary phases in Al<sub>x</sub>CoCrFeNi high-entropy alloys: an in-situ Tem heating study and thermodynamic appraisal, Acta Mater. 131 (2017) 206-220.
- Y. Ma, Q. Wang, B.B. Jiang, C.L. Li, J.M. Hao, X.N. Li, C. Dong, T.G. Nieh, Controlled formation of coherent cuboidal nanoprecipitates in body-centered cubic high-entropy alloys based on Al<sub>2</sub> (Ni,Co,Fe,Cr)<sub>14</sub>, compositions, Acta Mater, 147 (2018) 213-225.
- Q. Wang, Y. Ma, B.B. Jiang, X.N. Li, Y. Shi, C. Dong, P.K. Liaw, A cuboidal B2 nanoprecipitation-enhanced body-centered-cubic alloy Al<sub>0.7</sub>CoCrFe<sub>2</sub>Ni with prominent tensile properties, Scripta Mater. 120 (2016) 85–89.
- S. Allen, J.W. Cahn, Mechanisms of phase transformations within the miscibility gap of Fe-rich Fe-Al Alloys, Acta Met 24 (1976) 425-437.
- [41] D.B. Cullity, S.R. Stock, Elements of X-Ray Diffraction, third ed., Prentice Hall,
- America, 2001.
  Pandat<sup>TM</sup>, Thermodynamic Calculations and Kinetic Simulations. Compu-Therm LLC: Madison, WI - 53719.
- A.W. Funkenbusch, Discontinuous  $\gamma'$  coarsening in a Ni-Al-Mo base superalloy, Metall. Trans. A 14 (1983) 1283-1292.
- A. Picasso, A. Somoza, A. Tolley, Nucleation, growth and coarsening of  $\gamma'$ precipitates in a Ni-Cr-Al-based commercial superalloy during artificial aging, J. Alloys Compd. 479 (2009) 129-133.
- [45] A. Blachowski, S.M. Dubiel, J. Zukrowski, J. Cieślak, B. Sepiol, On the kinetics of the  $\alpha$ - $\sigma$  phase transformation in an Al-doped Fe-Cr alloy, J. Alloys Compd. 313 (2000) 182-187.
- [46] R.M. Vilar, G. Cizeron, Order disorder transition in Fe-Cr-phase, J. Mater. Sci. Lett. 2 (1983) 283-284.
- C. Zhang, F. Zhang, S. Chen, W. Cao, Computational thermodynamics aided high-Entropy alloy design, JOM 64 (2012) 839-845.

- [48] F. Zhang, C. Zhang, S.L. Chen, J. Zhu, W.S. Cao, U.R. Kattner, An understanding of high entropy alloys from phase diagram calculations, Calphad 45 (2014)
- [49] C. Zhang, F. Zhang, H. Diao, M.C. Gao, Z. Tang, J.D. Poplawsky, P.K. Liaw, Understanding phase stability of Al-Co-Cr-Fe-Ni high entropy alloys, Mater. Des. 109 (2016) 425-433.
- [50] R. Feng, M.C. Gao, C. Zhang, W. Guo, J.D. Poplawsky, F. Zhang, J.A. Hawk, J.C. Neuefeind, Y. Ren, P.K. Liaw, Phase stability and transformation in a lightweight high-entropy alloy. Acta Mater. 146 (2018) 280–293.
- [51] P.W. Voorhees, G.B. Mcfadden, W.C. Johnson, On the morphological development of second-phase particles in elastically-stressed solids. Acta Metall. Mater. 40 (1992) 2979-2992.
- [52] P. Fratzl, O. Penrose, LL. Lebowitz, Modeling of phase separation in alloys with coherent elastic misfit, J. Stat. Phys. 95 (1999) 1429–1503.
- [53] M.E. Thompson, C.S. Su, P.W. Voorhees, The equilibrium shape of a misfitting precipitate, Acta Metall. Mater. 42 (1994) 2107–2122.
- E.A. Marquis, D.N. Seidman, Nanoscale structural evolution of Al<sub>3</sub>Sc precipitates in Al(Sc) alloys, Acta Mater. 49 (2001) 1909–1919.
- R.J. Wasilewski, Elastic constants and young's modulus of NiAl, Trans. Mct.Soc. AIME 236 (1996) 455.
- T. Hong, A.J. Freeman, Effect of antiphase boundaries on the electronic structure and bonding character of intermetallic systems: NiAl, Phys. Rev. B: Condensed Matter, 43 (1991) 6446-6458.
- R. Kikuchi, J.W. Cahn, Theory of interphase and antiphase boundaries in F.C.C. allov, Acta Metall. 27 (1979) 1337–1353.
- [58] A.J. Ardell, Precipitation hardening, Metall Trans A 16A (1985) 1985–2135.
- A. Argon, Strengthening Mechanisms in Crystal Plasticity, Oxford University Press, Oxford, the United Kingdom, 2007.
- V. Gerold, H. Haberkorn, On the critical resolved shear stress of solid solutions containing coherent precipitates, Phys. Stat. Sol 16 (1966) 675-684.
- [61] B. Jansson, A. Melander, On the critical resolved shear stress from misfitting particles, Scripta Metall. 12 (1978) 497-498.
- A. Melander, P.A. Persson, The strength of a precipitation hardened AlZnMg alloy, Acta Metall. 26 (1978) 267-278.
- E. Nembach, Precipitation hardening caused by a difference in shear modulus
- between particle and matrix, Phys. Stat. Sol. 78 (1983) 571-581. W.F. Hosford, Mechanical Behavior of Materials, first ed., Cambridge Univer-
- sity Press, New York, America, 2005. E. Orowan, Symposium on Internal Stress in Metals and Alloys, Institute of
- Metals, London, 1948, pp. 451-453.
- L.M. Brown, R.K. Ham, Dislocation-particle interactions, in: A. Kelly, R.B. Nicholson (Eds.), Strengthening Methods in Crystals, Elsevier, Amsterdam, 1971, pp. 9-135.
- E. Nembach, Particle strengthening of metals and alloys, Mater. Sci. Technol. 3 1997) 329-337.
- ASM International Handbook committee, Properties and Selection: Irons, Steels and High Performance Alloys, second ed., vol. 1, ASM International, America, 1993.